PCCP

ROYAL SOCIETY OF CHEMISTRY

PAPER

Cite this: *Phys. Chem. Chem. Phys.*, 2023, **25**, 17558

A multi-physical quantity sensor based on a layered photonic structure containing layered graphene hyperbolic metamaterials

Jie Xu, Zhao Tang, You Ran Wu and Hai Feng Zhang *

Received 28th April 2023,
Accepted 6th June 2023

DOI: 10.1039/d3cp01944f

rsc.li/pccp

The layered photonic structure (LPS) sensor presented in this paper utilizes the intrinsic absorption principle of graphene which can improve the absorption rate by stacking layers to generate an absorption peak within the terahertz (THz) frequency range. The absorption peak can be used for multi-dimensional detection of glucose solution, alcohol solution, the applied voltage of graphene, the thickness of hyperbolic metamaterials (HMs), and room temperature. LPS is endowed with characteristics of a Janus metastructure through the non-stacked arrangement of different media and can have different sensing properties when the electromagnetic waves (EWs) are incident forward and backward. The Janus metastructure features in the forward and backward direction make it have different physical characteristics, forming sensors with different resolutions and qualities, so as to realize the detection of multiple physical quantities. One device has the detection performance of multiple substances, which greatly improves the utilization rate of the design structure. Furthermore, the addition of HM to the sensor structure enables it to exhibit angle-insensitive characteristics in both forward and backward directions. To further enhance the sensor's performance, the particle swarm optimization (PSO) algorithm is used to optimize structural parameters. The resulting sensor exhibits excellent sensing performance, with a high sensitivity (*S*) of 940.34 THz per RIU and quality factor (*Q*) and figure of merit (FOM) values of 37 4700 RIU^{-1}, respectively, when measuring voltage. For glucose and alcohol solutions, the sensor demonstrates *S* values of 5.52 THz per RIU and 4.44 THz per RIU, *Q* values of 8.3 and 37.2, and FOM values of 6.2 RIU^{-1} and 20.2 RIU^{-1}, respectively in different directions.

1. Introduction

A layered photonic structure (LPS) is a structure arranged by multiple media in a certain order in space, which can be accurately controlled by photons. LPS exhibit unique physical properties, such as photonic bandwidth and energetic locality, that make them ideal for use in a variety of research fields.[1,2] LPS-based components, such as retarders, polarizers, and sensors, have demonstrated superior performance.[3–5] In a previous study, LPS could be combined with the principle of optical Tamm state binding or defect films to make a sensor. The local area of the electric field produces sharp absorption peaks, and, because of the change of the measured amount, the phase of the electromagnetic waves (EWs) propagating in the whole structure is affected, resulting in the frequency shift of the absorption peaks, which can be used to detect viruses, gases, and other substances, and their smaller size makes them easier to be produced.[6,7] Janus metastructures derive their name from an ancient Roman story about a god with two faces looking in two directions, one into the past and the other into the future.[8,9] Similarly, for a sensor, different physical characteristics in different directions can greatly aid practical applications and greatly improve the device efficiency.[10] Therefore, combining the Janus principle, a sensor can be used to sense different physical quantities. When the sensor has the advantage of multi-physical quantity measurement, it can be applied more widely. The limitation of sensor measurement determines its low efficiency.

Traditional sensor designs can only work effectively when the signal source is obliquely incident at a specific angle. However, in actual production, the product's jitter may not meet such strict requirements, and even a slight change in angle can significantly weaken the sensor's performance or cause detection errors. To address these issues, this paper delves deeper into two-dimensional materials science,[11–14] and principles to identify an unknown material that can induce the principle of phase matching: hyperbolic metamaterial (HM).[15–17] These materials exhibit high anisotropy in their electromagnetic properties. Anisotropic composite electromagnetic materials can be created by stacking metals and graphene with a dielectric substrate, as reported in previous studies.[18–20] HM's unique near-field

College of and Optical Engineering & College of Flexible Electronics (Future Technology), Nanjing University of Posts and Telecommunications, Nanjing, 210023, China. E-mail: hanlor@163.com

manipulation of EWs in the terahertz (THz) range makes it a promising material for increasing the photon density and enhancing spontaneous emission which can achieve phase matching within a certain range, ensuring that the sensor's physical properties are not interfered with when incident at a wide angle.[21–24] Equally hot is the design of Janus sensors, which can reflect different physical characteristics in different directions, and are proposed to produce logical gates with sensing functions and structural colors.[25,26] As a result, an angle-insensitive and multifunctional sensor can be produced, significantly expanding the application scenarios for sensor technology.

The transfer matrix method (TMM) is an important tool for the multi-dimensional calculation of LPS in previous studies.[27] The absorption rate, reflectivity, and other attributed parameters of the design structure can be obtained through complex high-latitude calculations. As early as 1995, James Kennedy and Russell Eberhart developed a simplified algorithm model known as particle swarm optimization (PSO), inspired by the regularity of bird foraging behavior, which has become a powerful tool for speeding up computation and realizing multi-dimensional computations.[28] The PSO algorithm often coordinates with TMM, so that it can dynamically adjust the parameters of the LPS to compare the absorption rate.[29]

By improving the PSO, an ameliorated PSO (APSO) algorithm is obtained to further optimize the structure so that our study presents a groundbreaking wide-angle insensitive sensor that harnesses the intrinsic absorption of graphene. Based on the hidden Markov model and the phase change compensation effect between the medium, an angle-independent gap is realized,[30] which can be used as the placement layer of the object to be measured, greatly improving the application of the sensor in practical situations. The stability of the incident angle is obtained, remaining steady within a range of 0–60° while maintaining an exceptional absorption rate of 0.9 or higher at a single frequency point. The proposed innovative design features a specially designed chamber to hold glucose (G) and adjust dimensions for precise sensing measurements. In testing the proposed LPS, this paper utilizes G solutions ranging from 4% to 74.7% in concentration, achieving remarkable results. The given sensor boasts a sensitivity (S) value, quality factor (Q), and figure of merit (FOM) of 5.52 THz per RIU, 8.3, and 6.2 RIU^{-1}, respectively. In addition, the designed LPS demonstrated outstanding performance in the measurement of thickness and graphene applied voltage, with a splendid S value of 940.34 THz per RIU and Q and FOM values of 37, 4700 RIU^{-1}. When the EWs are incident backward, the sensing performance is even more accurate, with the range of angular instability extending to 0–72.5°. The sensor can distinguish five alcohol groups in alcohol solution, including methanol, ethanol, propanol, butanol, and phenol, with an S value of 4.44 THz per RIU, Q of 37.2, and FOM of 20.2 RIU^{-1}, ensuring the response and accuracy of alcohol measurement. The voltage measurement is the most prominent performance, with an S value of 940.34 THz per RIU, and Q and FOM of 37,4700 RIU^{-1}. Unlike when EWs spread forward, the reverse stacking of media in LPS can detect external temperature ($T_{External}$) changes through the change of absorption rate, which holds practical application significance.

2. Design and discussion

2.1. Theoretical model

The angle-insensitive LPS proposed is a multifunctional sensing structure consisting of 29 media stacks (as shown in Fig. 1). The structure employs a HM consisting of graphene combined with a dielectric material with a constant of 1.1. Here, the thickness d_C of the dielectric material is 300 nm, and the thickness of G, d_G is set as 0.34 nm. The refractive indices (RIs) of lead dioxide (PbO_2) and silicon (Si) are constant at 2.3 and 4.2, respectively, and in the range of THz operating frequency, the refractive index (RI) is not affected by frequency change. M_1, M_2, and M_3 respectively represent the LPS of three different materials. HM, PbO_2, and Si

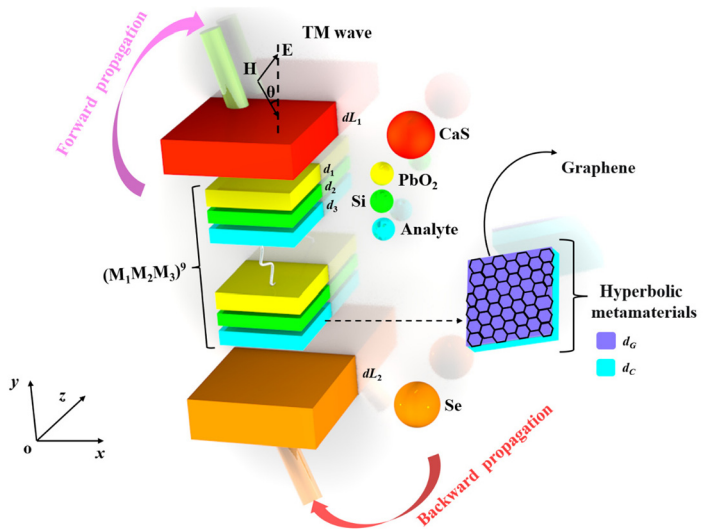

Fig. 1 The structure atlas of angle-insensitive LPS.

come together to form a periodic structure with thickness of d_1 = 910 nm, d_2 = 280 nm, and d_3 = 300 nm, achieving stability in the face of diverse angles. In a bid to further strengthen the performance of the sensor, calcium sulfide (CaS) metal (n = 2.1) with a thickness of dL_1 = 18 μm and cesium (Se) (n = 2.8) with a thickness of dL_2 = 2.8 μm are added on both sides of the periodic structure. In this study, the proposed structure is designed to allow for the entry of EWs in the form of transverse magnetic (TM) waves. TM waves are characterized by having an electric field component but no magnetic field component in the direction of propagation, with the direction of the electric field being perpendicular to the direction of propagation.

2.2. Calculation method

2.2.1 TMM. TMM is utilized to calculate the absorption rate of the HM structure used in this paper, which combines graphene with a normal medium.[31] The relevant formula is derived as follows. The conductivity of graphene differs significantly from that of ordinary media, and its wavelength dependence can be expressed using the following eqn (1)[32]

$$\sigma = \frac{ie^2 k_B T_{External}}{\pi\hbar^2(\omega + i/\tau)}\left(\frac{\mu_c}{k_B T_{External}} + 2\ln\left(e^{-\frac{\mu_c}{k_B T_{External}}} + 1\right)\right) + \frac{ie^2}{4\pi\hbar}\ln\left|\frac{2\mu_c - \hbar(\omega + i/\tau)}{2\mu_c + \hbar(\omega + i/\tau)}\right|, \quad (1)$$

where $e = 1.6 \times 10^{-19}$ C is the electron charge, $K_B = 1.380649 \times 10^{-23}$ is the Boltzmann constant, initially set at 279 K, and $\hbar = 1.05457266 \times 10^{-34}$ J·s is the reduced Planck constant, ω represents the angular frequency of the incident EWs, τ stands for the scattering rate of electron. μ_c is the chemical potential, related to the applied voltage V_g, and can be written as eqn (2)[33]

$$|\mu_c| = \hbar\nu_F\sqrt{\pi|k_0(V_g - V_D)|}, \quad (2)$$

where $\nu_F = 10^6$ m s^{-1} corresponds to the Fermi velocity of graphene,[34,35] $k_0 = 9.1016$ m^{-1} V^{-1}. V_D is the offset bias voltage and is assumed to be 0 V. By exploring the formula for calculating the dielectric constant of graphene materials, the effective dielectric constant can be expressed as below when it is not affected by other external environmental factors:[33]

$$\varepsilon_G = 1 + \frac{i\sigma}{\omega\varepsilon_0 d_G}, \quad (3)$$

$$\varepsilon = \begin{pmatrix} \varepsilon_{xx} & 0 & 0 \\ 0 & \varepsilon_{yy} & 0 \\ 0 & 0 & \varepsilon_{zz} \end{pmatrix}, \quad (4)$$

$$\varepsilon_{xx} = \varepsilon_{yy} = \varepsilon_p = \frac{\varepsilon_G d_G + \varepsilon_C d_C}{d_G + d_C}, \quad (5)$$

$$\varepsilon_{zz} = \varepsilon_v = \frac{\varepsilon_G \varepsilon_C (d_G + d_C)}{\varepsilon_G d_C + \varepsilon_C d_G}, \quad (6)$$

The dielectric constant of graphene materials can be calculated using the formula presented above, where $\varepsilon_0 = 8.854187817 \times 10^{-12}$ F m^{-1} is the dielectric constant in a vacuum, and d_G represents the thickness of graphene, which is 0.34 nm. Since the HM structure of graphene is an anisotropic medium and has a uniaxial dielectric tensor component, the dielectric constant of graphene in each direction can be expressed using the parallel component, ε_p, and the vertical component, ε_v[36]

$$n_g = \sqrt{\frac{\varepsilon_v^2}{\varepsilon_p} - \frac{\varepsilon_v}{\varepsilon_p}\left(1 - \frac{\varepsilon_p}{\varepsilon_v}\right)\sin^2\theta}. \quad (7)$$

Then, the RI calculation formula derived from Snell's law is shown above and the dielectric constant data obtained above can be combined to get the equivalent n_g when the incident angle is θ (see Fig. 1). The transfer matrix can be expressed as[37]

$$M_{o=1\ldots29} = \begin{pmatrix} \cos\delta_o & -\frac{i}{\eta_o}\sin\delta_o \\ -i\eta_o\sin\delta_o & \cos\delta_o \end{pmatrix}, \quad (8)$$

where $\eta_o = n_o\cos\theta_o$, $\delta_o = \omega n_o d_o \cos\theta_o/c$, n_o represents the RI of layer o, d_o, and θ_o on behalf of the thickness and incidence angle of layer o, respectively. The overall transfer matrix of the designed angle-insensitive structure can be written as[37]

$$M = \sum_i^{29} M_i = \begin{pmatrix} M_{11} & M_{12} \\ M_{21} & M_{22} \end{pmatrix}. \quad (9)$$

The reflection coefficient r and transmission coefficient t are calculated by the following formula for the four elements in the two-dimensional matrix obtained by TMM.[37]

$$r = \frac{(M_{11} + M_{12}\eta_{air})\eta_{air} - (M_{21} + M_{22}\eta_{air})}{(M_{11} + M_{12}\eta_{air})\eta_{air} + (M_{21} + M_{22}\eta_{air})} \quad (10)$$

$$t = \frac{2\eta_{air}}{(M_{11} + M_{12}\eta_{air})\eta_{air} + (M_{21} + M_{22}\eta_{air})} \quad (11)$$

When the EWs are incident at TM waves, $\eta_{air} = n_{air}/\cos\theta_{air}$, n_{air} describes the RI of air. Reflectance (R) and transmittance (T) are $R = r\cdot r^*$ and $T = t\cdot t^*$. r^* and t^* stand for taking the conjugate function of the corresponding variable. The absorption rate A can be written as

$$A = 1 - R - T \quad (12)$$

2.2.2 APSO algorithm. The conventional approach to enhancing sensor parameters involves the enumeration method, which involves testing all possible material parameters and comparing their sensing performance. This method, however, is time-consuming and may not guarantee optimal results. To address this, the authors of this paper employed the APSO algorithm, as depicted in Fig. 2. By programming the computer to independently optimize structural parameters, this approach significantly improves time efficiency and facilitates the identification of the accomplished optimization resulting from a vast amount of data, as compared to manual adjustment optimization.

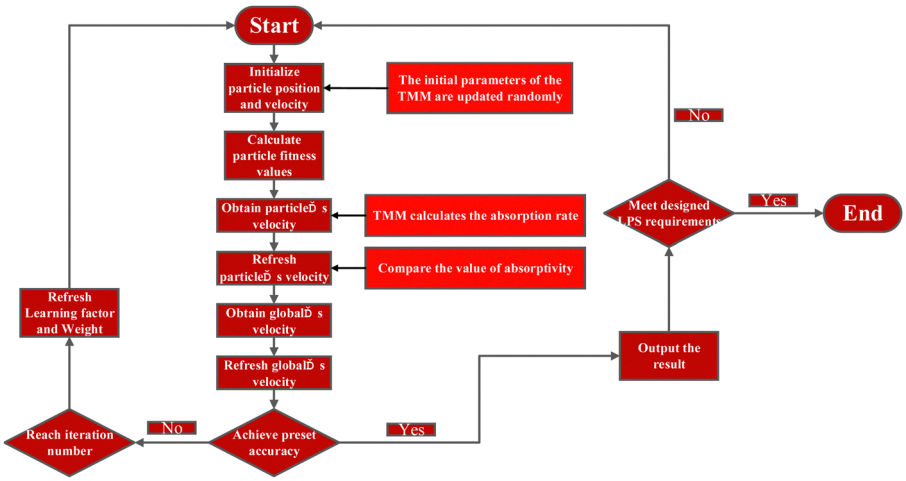

Fig. 2 APSO procedure step diagram.

The calculation principle of APSO is analyzed, and its core calculation formula is shown as follows:[38]

$$\begin{cases} X_{k+1}(w) = X_k(w) + V_k(w) \\ V_{k+1}(w+1) = \mathrm{i}V_k(w) + \sum_{p_i \in N_k} c_i r_i (P_i(w) - X_k(w)) \end{cases} \quad (13)$$

$$w = 1, 2, \ldots, W_F, k = 0, 1, 2 \ldots D$$

where W_F, D, $X(w)$, and $V(w)$ respectively represent the number of particle swarms, the number of formula iterations, and the position and direction velocity vector of particles. $P(w)$ is used for the optimal position of the storage space. After each iteration, an individual optimal position $P_{\mathrm{indi}}(w)$ will be obtained. At the end of an iteration, the individual optimal position will be compared with the current global optimal position $P_{\mathrm{gro}}(w)$. i represents the inertia factor, and c_i stands for the learning factor. The magnitude of these two parameters will affect the relationship between the speed of adjacent iterations, thus affecting the generation and selection of the optimal position. The method of adjusting learning factors used in this paper is the asynchronous automatic adjustment method, which can give the algorithm with a stronger ability to get rid of local optimal results; in other words, it has a stronger ability to find optimal results. eqn (14) and (15) are as follows.[39]

$$c_1 = c_{1.\mathrm{start}} + (c_{1.\mathrm{end}} - c_{1.\mathrm{start}})\frac{G}{M}, c_{1.\mathrm{start}} = 2.5, c_{1.\mathrm{end}} = 0.5 \quad (14)$$

$$c_2 = c_{2.\mathrm{start}} + (c_{2.\mathrm{end}} - c_{2.\mathrm{start}})\frac{G}{M}, c_{1.\mathrm{start}} = 0.5, c_{1.\mathrm{end}} = 2.5 \quad (15)$$

2.2.3 Sensing performance calculation. The materials and principles involved in sensor manufacturing are diverse, but the comparative scale used to describe sensing performance is typically more unified. Three important metrics used for this purpose are S, Q, and FOM. The formulas for calculating these metrics are given in eqn (16)–(18), respectively:[40]

$$S = \frac{\Delta f}{\Delta n}, \quad (16)$$

$$Q = \frac{f_T}{\mathrm{FWHM}}, \quad (17)$$

$$\mathrm{FOM} = \frac{S}{\mathrm{FWHM}}, \quad (18)$$

where Δf and Δn stand for the amount of variation in frequency and RI, f_T represents the magnitude of the peak frequency, full width at half maxima (FWHM) on behalf of the half-high frequency width of the absorption peak or transmission one.

2.3. Analysis and discussion

In this study, the APSO algorithm is used to optimize 12 structural parameters that represent different materials in the designed structure, namely thickness, RI, μ_c, and T_{External} of LPS. Careful consideration is given to determining the appropriate value ranges for these optimization parameters, striking a balance between minimizing the algorithm's runtime and maintaining physical significance. The initial population size for the optimization algorithm is set to 300, with a total of 4000 iterations. At each iteration, the absorption rate is calculated and compared to obtain data such as those presented in Table 1.

The number of graphene layers is crucial as it directly impacts the properties and characteristics of graphene. It determines whether graphene is a single-layer (monolayer), few-layered, or multi-layered material, with significant implications for its electrical, optical, mechanical, and thermal properties. Additionally, the number of layers affects the band structure, electronic bandgap, carrier mobility, and integration potential of graphene in electronic, optoelectronic, and energy-related applications. Understanding and controlling the number of graphene layers enable tailored properties and optimized performance for specific uses. In Fig. 3(a), when EWs are incident from the forward direction, our study focused on a narrower frequency band (9–10.5 THz) and observed that increasing the number of graphene layers resulted in a shift of the absorption peak from high to low frequencies. However, the overall absorption profile

Table 1 The comparative evaluation of different works

Parameter	Range	Optimization result	Parameter	Range	Optimization result
d_1 (nm)	$10–10^5$	910	n_1	1–5	2.3
d_2 (nm)	$10–10^5$	280	n_2	1–5	4.2
d_3 (nm)	$10–10^5$	300	n_3	1–5	1.21
dL_1 (nm)	$10–10^5$	1800	nL_1	1–5	2.1
dL_2 (nm)	$10–10^5$	2800	nL_2	1–5	2.8
μ_c (eV)	0–1	0.102	$T_{External}$ (K)	200–300	279

remained relatively unchanged. In Fig. 3(b), within the range of 6.50–7.50 THz, we observe a consistent shift in the absorption peak as the number of graphene layers varied from 1 to 10. However, when the number of layers increased to 100, the absorption spectrum no longer exhibited a single peak but showed a band distribution of high absorption. Considering the observed changes and the relationship between the number of graphene layers, our design in this study focuses solely on incorporating a single-layer graphene structure.

Based on the real part of the graphene HMs' $\varepsilon_{\parallel}$ and epsilon at different frequencies, as shown in Fig. 3(c) and (d), it is observed that $\varepsilon_{\parallel}$ increases from negative to positive values in the frequency domain, with the majority of values being negative within the operating frequency range. The real part of the $\varepsilon_{\perp}$ remains stable at around 1.10 throughout the terahertz frequency range. It is well-known that materials with $\mathrm{Re}(\varepsilon_{\parallel})\mathrm{Re}(\varepsilon_{\perp}) < 0$ have hyperbolic properties, while those with $\mathrm{Re}(\varepsilon_{\parallel})\mathrm{Re}(\varepsilon_{\perp}) > 0$ have conventional dielectric properties similar to common dielectric materials. From Fig. 3, it can be observed that the material properties change from hyperbolic to ordinary dielectric in the operating frequency range.

The periodic structure plays a crucial role in achieving a transmittance greater than 0.9. As depicted in Fig. 4(a), the absorption rate of a single-layer periodic structure is only 0.223, and when the EWs are incident from the back, the absorption rate can only reach 0.4071 (as shown in Fig. 4(b)). However, as shown in Fig. 4(c) and (d), the dielectric constant of graphene varies within the working frequency, and due to the superposition of intrinsic absorption of graphene, the absorptivity of the front and back sides of the structure is observed simultaneously. With the adjustment of the periodicity to 9, the absorptivity of the front and back of the structure can be significantly increased to 0.985 and 0.9845, respectively (as shown in Fig. 4(e) and (f)). For the forward direction of EWs, the peak frequency point of the intrinsic absorption map of graphene was selected to perform the angle-insensitive test at 10 THz. This choice is motivated by the fact that the sensor designed in this study relies on the peak absorption rate of the material. In contrast, for the backward direction of incident EWs, 7.3 THz is chosen as the angle-insensitive test point following the same principle. By incorporating HM, the design structure achieves large angular stability in the front and rear directions, respectively, within 0–60° and 0–72.5°. Consequently, the excellent physical characteristics can be reasonably utilized in the sensor parts, maintaining excellent transmittance in the range of 120° and 150° when light is transmitted from the front and rear directions, respectively, as shown in Fig. 5(a) and (b).

The design structure based on the intrinsic absorption principle of graphene achieves high absorptivity greater than 0.9 in both forward and backward directions, displaying angle-insensitive characteristic frequencies as shown in Fig. 6. The blue peaks represent the result of EWs incident from the forward

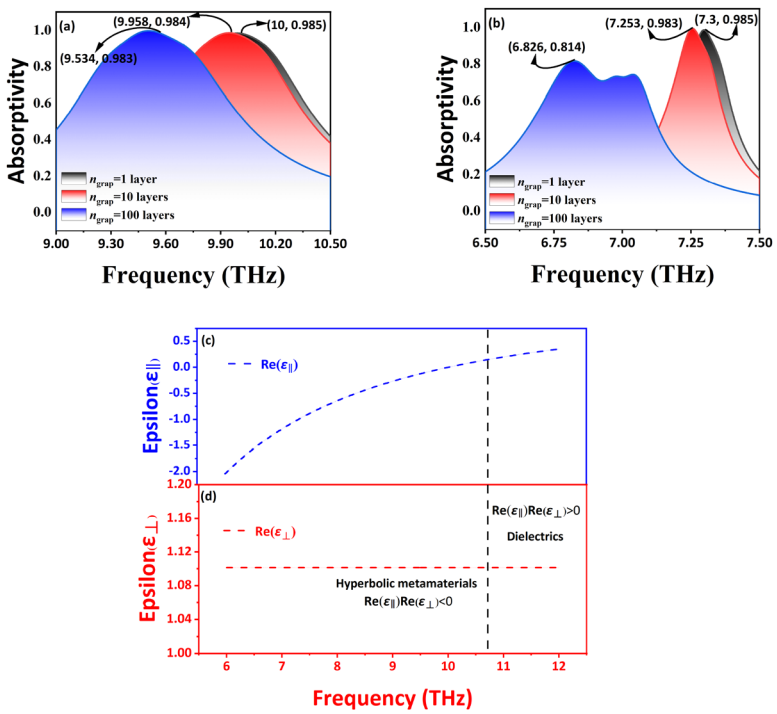

Fig. 3 The discussion of graphene layer number, (a) forward and (b) backward. The real parts of $\varepsilon_{\parallel}$ (c) and $\varepsilon_{\perp}$ (d) of the HMs with graphene.

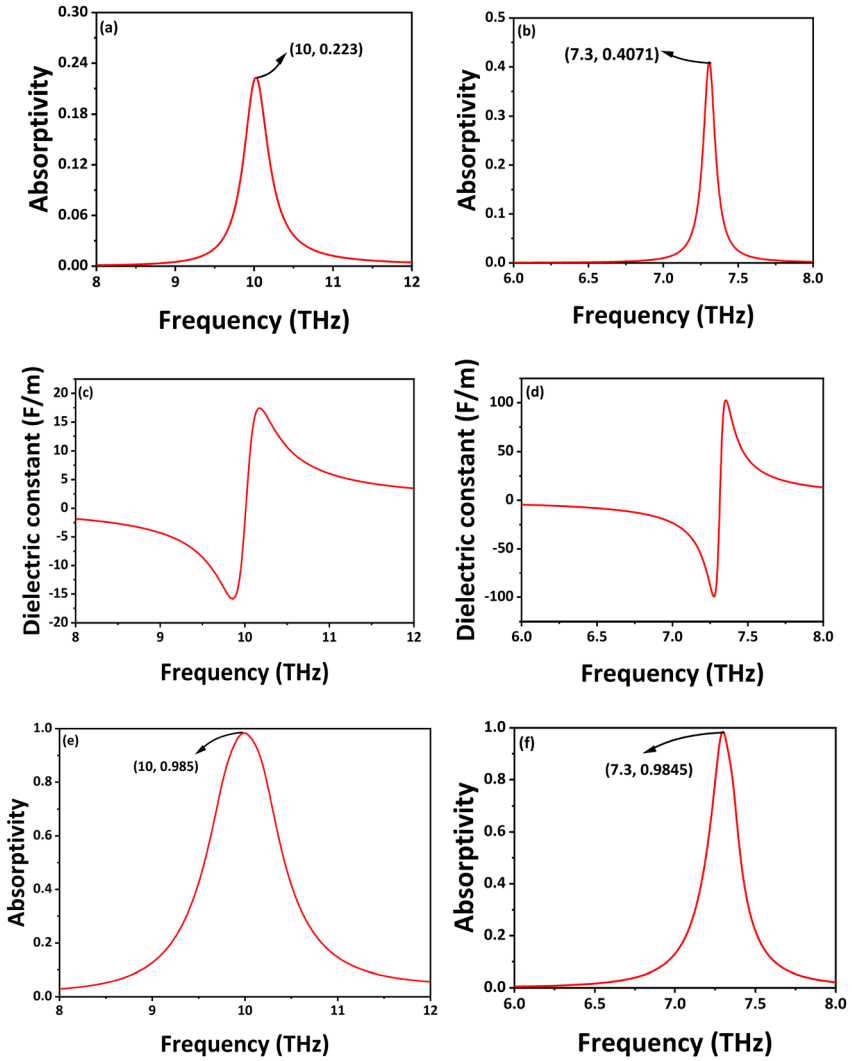

Fig. 4 (a) Forward incident a single-layer graphene absorption rate. (b) Backward incident single-layer graphene absorption rate. (c) Relationship between the permittivity of forward incident graphene and its operating frequency. (d) Relationship between the permittivity of backward incident graphene and its operating frequency. (e) Absorption rate of forward incident 9-layer graphene. (f) Absorption rate of backward incident 9-layer graphene.

direction, while the red peaks represent the result of EWs incident from the opposite direction. Furthermore, the range of 6–12 THz shows no miscellaneous peak greater than 0.1, demonstrating excellent absorptivity performance that is essential in sensor design.

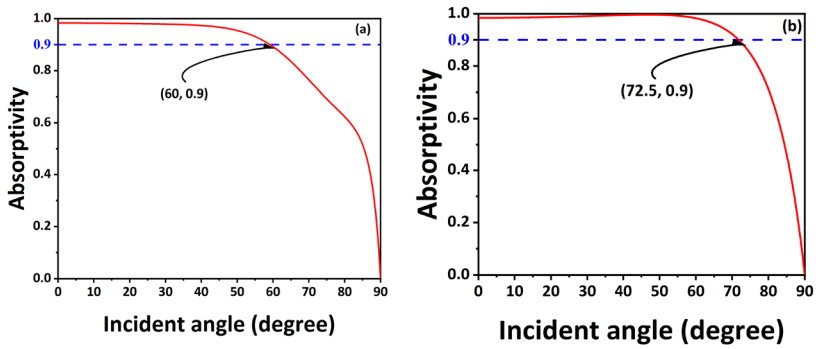

Fig. 5 (a) The absorption rate of each angle at the frequency of 10 THz at forward incidence. (b) The absorption rate of each angle at the frequency of 7.3 THz at backward incidence.

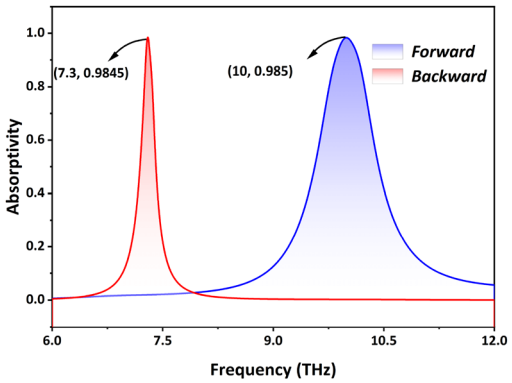

Fig. 6 The absorption peaks of forward and backward incidence in the operating frequency range respectively.

To further verify the validity of our theoretical study, we conduct simulations of a graphene-based LPS. The LPS is designed based on the intrinsic absorption principle of graphene and is tested in both forward and backward directions. The results show that the LPS maintained a high absorption rate of over 0.9 while remaining insensitive to a single frequency point with a large angle. The magnetic field intensity distribution in the *z*-direction depicts the behavior of the incident TM wave's magnetic field intensity at the corresponding frequency of the transmission peak. The magnetic field distribution obtained from the simulation is consistent with our theoretical predictions, as shown in Fig. 7(a). It is observed that the magnetic field values are at a minimum at the incident end of the EWs, whereas the maximum magnetic field values are obtained at the first, fifth, and ninth layers of the periodic structure during the transmission of the EWs in the structure. Finally, the EWs exit the last layer of the metal structure with a relatively stable high value of the magnetic field. When the EWs are incident in the opposite direction, the design structure still shows a significant periodic electric field distribution, as depicted in Fig. 7(b). Similar to the forward incident case, the structure exhibits three electromagnetic maxima. In the distribution of other media, the magnetic field sharply decreases, with blue representing low values and red representing high values.

Upon examining the curve shape in Fig. 8(a), it is evident that the relationship between frequency and absorption rate is

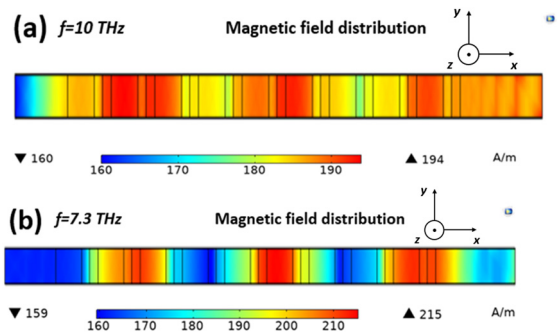

Fig. 7 Simulation results of magnetic field sizes of sensing structures at various locations (a) the forward propagation, and (b) the backward propagation.

consistent between the five thickness measurement points, with peak absorption rates exceeding 0.9, nearing 1. This fundamental principle is integral in the developed sensors. Simulations are carried out to calculate the absorption rate at each frequency point within the thickness range, yielding the three-dimensional results shown in Fig. 8(b). Notably, absorption rates of nearly 1 are observed at all space points between 9 THz and 10.3 THz, while other frequency ranges displayed a rapid decline in the absorption rate. Linear fitting of the five frequency points is conducted separately, as depicted in Fig. 8(c), with S = 15 THz μm^{-1} and R^2 = 0.998, verifying a close linear relationship between the five points, $f = -15d + 14.179$, it provides a benchmark for the manufacture of sensors. The average values of Q and FOM are 11.69 and 18.56 RIU^{-1} are revealed in Fig. 8(d), respectively, with maximum values observed at a thickness of 0.32 μm, exhibiting a synchronous increase of Q and FOM.

The thickness sensor measurement can also be achieved when light is transmitted from the opposite direction, with a different working frequency band, as shown in Fig. 9(a). Within the frequency band of 6–8 THz, the measurement range spans from 0.09–0.13 μm. Remarkably, the measurement of the same physical quantity can demonstrate distinct qualities and properties. Fig. 9(b) portrays the three-dimensional architecture diagram of backward absorptivity, indicating that the frequency range with high absorptivity is narrower, implying a superior FWHM, and more distinctive color differentiation, displaying a certain trend distribution. A few measurement points are selected to examine the functional relationship, $f = -27.07d + 9.7011$ is shown in Fig. 9(c), with S as high as 27.07 THz μm^{-1} and R^2 maintained at 0.997, verifying the structure's foundation for sensor manufacturing. Fig. 9(d) confirms the exceptional sensing performance of the rear-facing structure, with maximum values for Q and FOM reaching 38 and 140.3 RIU^{-1}, with a slight decrease in value as thickness increases.

Fig. 10(a) shows that the absorption peak curve is smooth and complete without any burrs, proving the integrity of the structural design when the external μ_c is changed. Using the formula mentioned above, the relationship between applied voltage and μ_c can be established. Fig. 10(b) shows the absorptivity of each point in the entire working frequency band under different applied voltage conditions. The high and low absorption ranges can be distinguished by the cold and warm colors ranging from dark blue to red. Fig. 10(c) demonstrates the high-line relationship between the sensing structure and frequency change under applied voltage, $f = -260.6V + 7.528$. The value of S is 260.6 THz mV^{-1}, and the high-line relationship can be confirmed by R^2 = 0.998. The sensor performance remains superior, with the highest values of Q and FOM reaching 13.4 and 347.5 RIU^{-1} and the lowest values being 11.4 and 280.3 RIU^{-1} in Fig. 10(d).

When measured in the reverse, the structure still demonstrates the basis for achieving excellent voltage sensing characteristics, as shown in Fig. 11(a)–(c). The correlation linear fitting relation is $f = -940.3V + 6.323$. Compared to the forward direction, the range of applied voltage measured in the reverse is smaller, providing the structure with additional measurement possibilities. The direction of detection is chosen according to

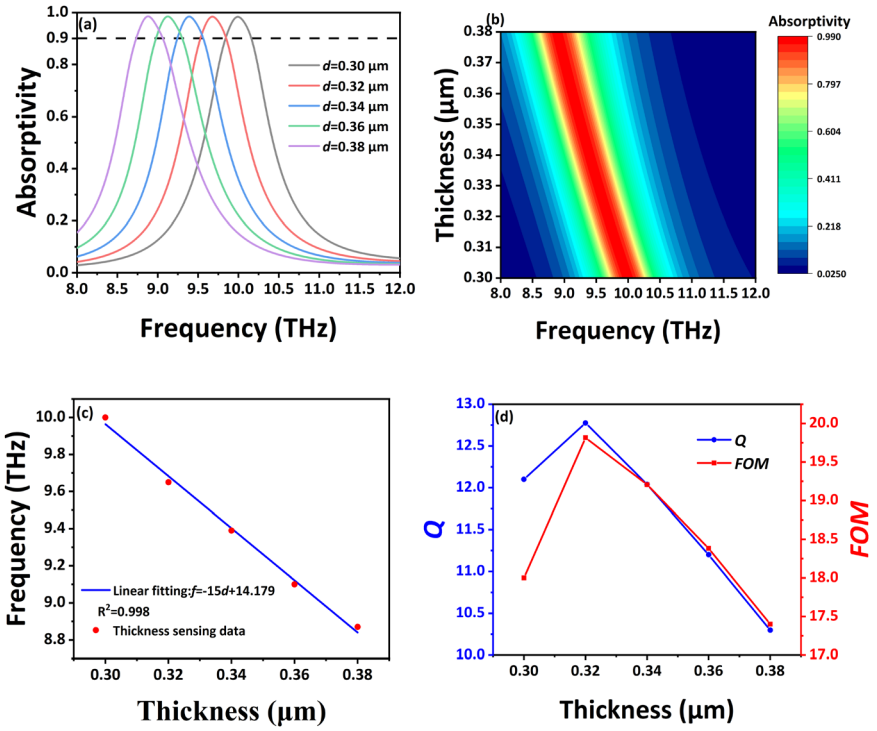

Fig. 8 (a) Forward thickness sensing of absorption at each frequency. (b) The absorption rate of each frequency within the working frequency range of the thickness sensor. (c) Curve fitting of frequency point movement of thickness variation (d) Performance index of thickness sensing in working frequency band.

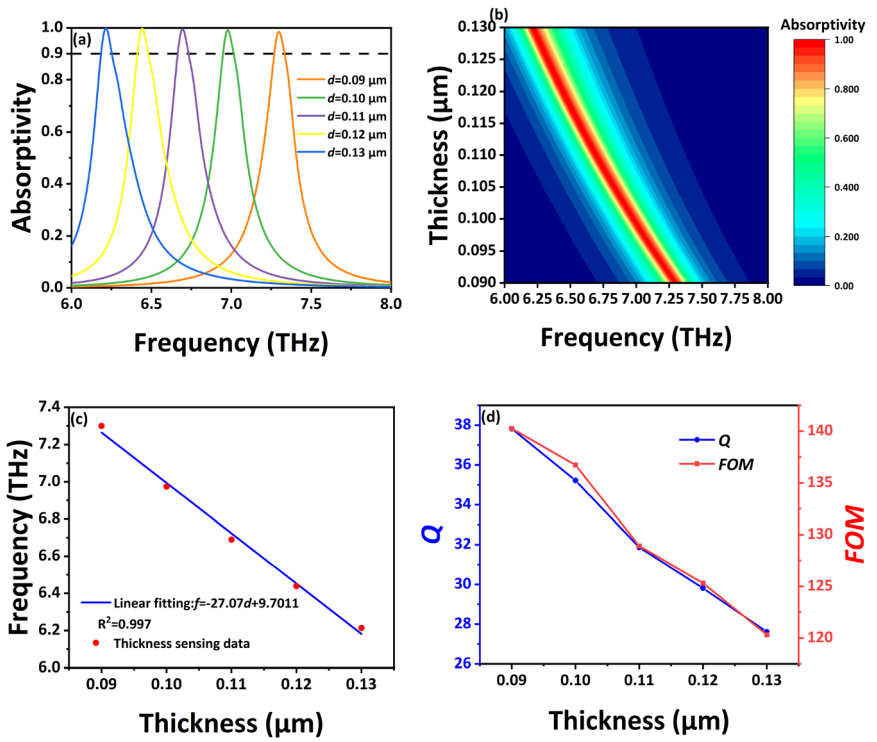

Fig. 9 (a) The operating frequency within the measurement range of backward thickness corresponds to the absorption rate. (b) The absorption rate at each frequency of the thickness. (c) The connection between thickness measurement points and frequencies. (d) Thickness sensor performance indicators *Q* and FOM.

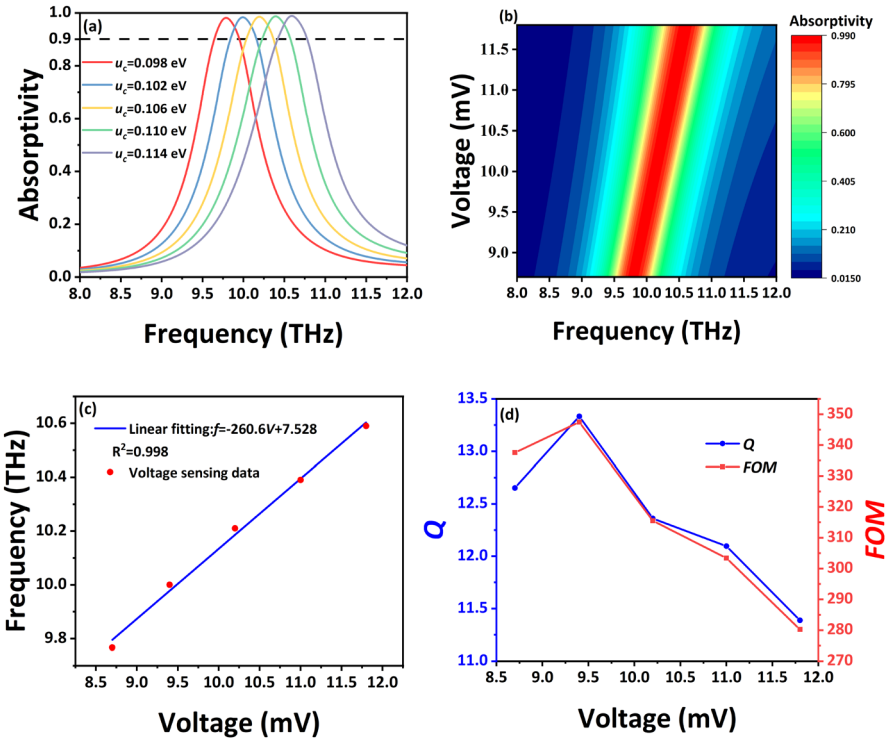

Fig. 10 (a) Frequency absorption curve under different μ_c conditions. (b) The absorption rate at each frequency of the applied voltage. (c) Curve fitting between selected points of equidistant voltage sensor measurement. (d) Voltage sensor performance indicators Q and FOM.

the applied voltage. Fig. 11(d) illustrates that the values of Q and FOM are relatively large, with the average value reaching 37,4700 RIU^{-1}, and the variation law slightly decreasing with an increase in the voltage. The performance in the reverse direction

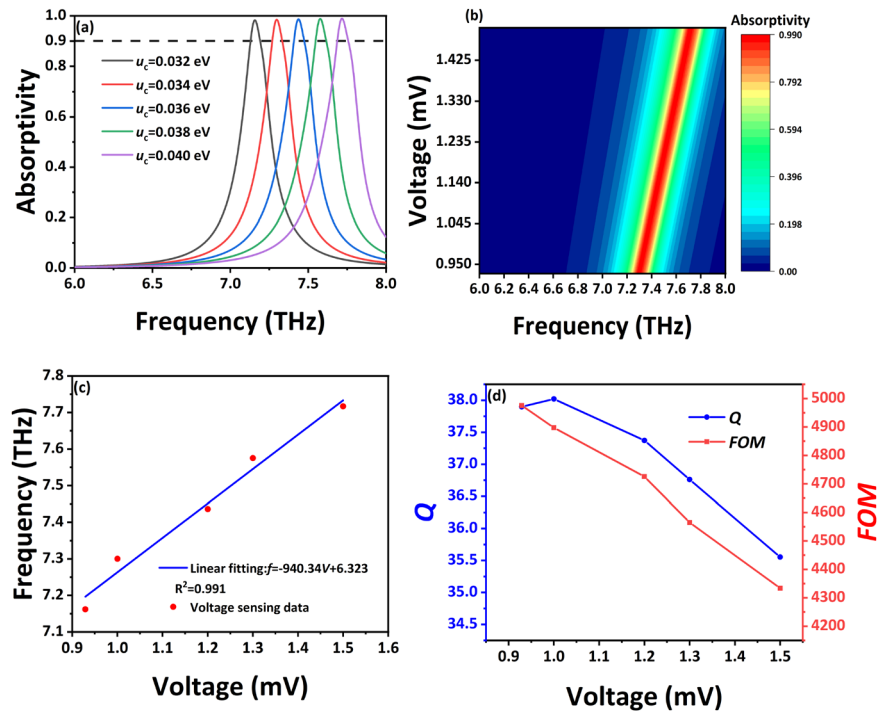

Fig. 11 (a) Backward incidence, absorption rate of each frequency at multiple μ_c values. (b) three-D diagram of frequency, voltage and absorptivity under applied voltage. (c) Explore the relationship between five measurement points selected in the measurement range. (d) The embodiment of voltage sensing performance.

is better, more stable, and provides more accurate and sensitive detection compared to the forward direction.

Sensing can be achieved in different voltage ranges in both forward and reverse directions. It is important to note that the voltage measurement spacing is intentionally small, indicating that the design structure is highly sensitive to voltage detection. Compared to general sensing techniques, high-S voltage detection is more accurate in material measurement, more responsive to changes in the medium, and can be advantageous in applications that require strict S requirements.

G solution sensors are crucial for monitoring blood G levels in individuals with diabetes. The urgency of G solution sensor research is high due to the significant and increasing prevalence of diabetes worldwide. According to the International Diabetes Federation, there were an estimated 463 million adults aged 20–79 with diabetes in 2019, and this number is expected to rise to 700 million by 2045.[41] The present study investigated the absorptivity of G aqueous solution and its relationship with the RI within the operating frequency range (see eqn (19)).[42] Fig. 12(a) depicts a smooth curve with high absorptivity values close to 1, obtained from five equally spaced measurement points ranging from 4% to 74.7%. The transmission of the G aqueous solution is represented in Fig. 12(b) by a color gradient from red to blue in a two-dimensional image of frequency and RI. The results show that the transmission is greater than 0.9 in the range of 7.3–8.1 THz and remain above 0.5 in the 7–8.5 THz range, with a declining trend outside the red and green regions. The strong linear relationship between measurement points and frequency lays the foundation for designing G sensors, as

Table 2 RI of various alcohol groups

Name of the alcohol	RI
Methanol	1.33
Ethanol	1.36
Propanol	1.38
Butanol	1.40
Phenol	1.53

indicated in Fig. 12(c) where an R^2 value of 0.999 is achieved in the linear fitting relationship with an S of 5.52 THz per RIU for G sensing. The data obtained are further utilized for measuring Q and FOM, with Fig. 12(d) showing that the maximum and minimum values of Q and FOM are 8.43, 6.53 RIU^{-1} and 8.09, 5.77 RIU^{-1}, respectively, with a range of 0.32 and 0.76.

$$n_G = 0.00011889C_G + 1.33230545 \quad (19)$$

Alcohol sensors are important for promoting public safety by detecting alcohol impairment in individuals, thereby reducing the risks of accidents, injuries, and fatalities.[43] Law enforcement officers rely on alcohol sensors to detect impaired driving, and inaccurate readings could have serious consequences for public safety, and the five different AL groups (see Table 2) investigated in this paper can often be challenging to differentiate.[44,45] Alcohol is a soluble substance. When different alcohol types are mixed into water, the difference in RI is generated. The proposed LPS structure is very sensitive to the change of RI and can feel the displacement phenomenon of absorption summit when RI changes within the range of working frequency. The proposed

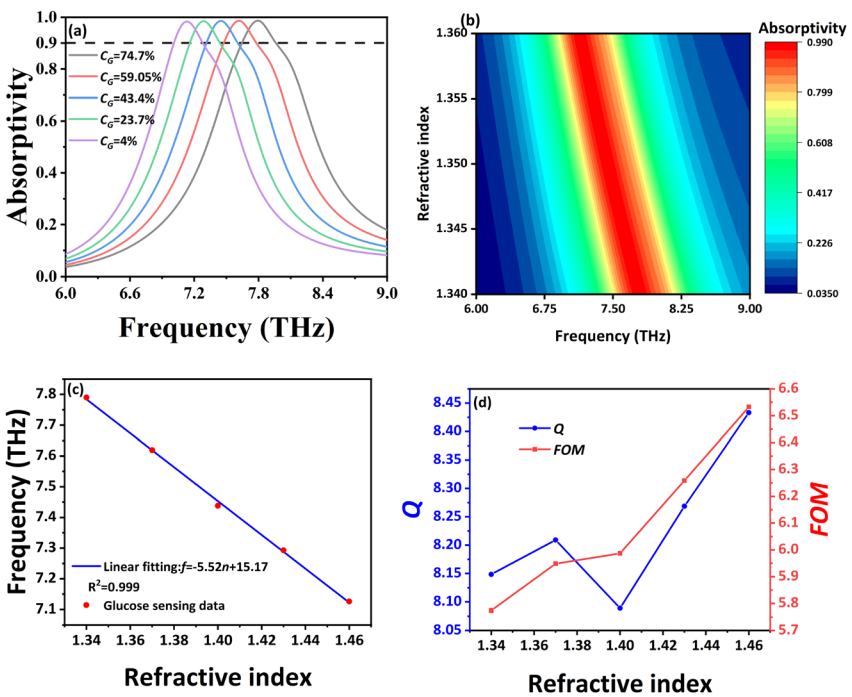

Fig. 12 (a) The absorption peak curve of each G solution concentration in the frequency range when forward incidence. (b) The absorption rate of the corresponding RI of the object to be measured at each frequency point. (c) The fitting curve of the frequency corresponding to the equivalent RI of the object to be measured. (d) Performance demonstration of G sensing.

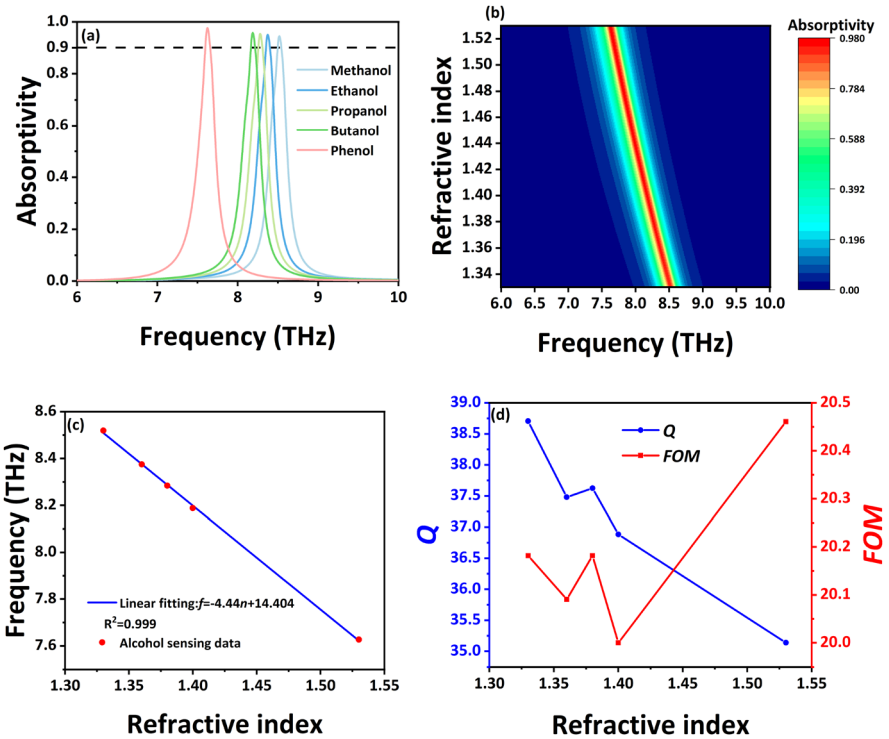

Fig. 13 (a) When EWs are incident in the reverse direction, the absorption rate of the five alcohols within the working frequency band was designed. (b) The absorption distribution of RI of the AL-based equivalent substance is analyzed in the working range of the sensor. (c) Curve relationship between frequency of five alcohols and corresponding RI. (d) The sensing properties of the sensor are characterized by evaluating the *Q* and FOM values for five alcohols.

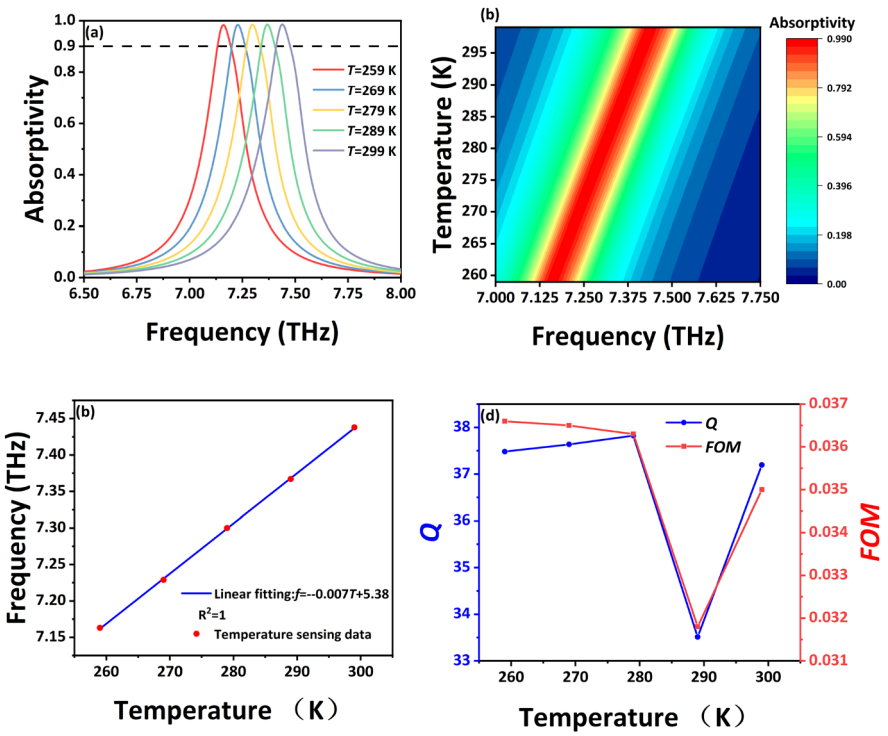

Fig. 14 (a) The influence of $T_{External}$ on the frequency absorption curve of the design structure. (b) Within the working frequency, the absorption rate of each point when $T_{External}$ varies from 259 K to 299 K. (c) The relationship between change of $T_{External}$ and frequency of corresponding absorption peak. (d) The corresponding sensing performance values *Q* and FOM are obtained in the range of $T_{External}$ variation.

Table 3 The performance of published literature reports compared with this work

Literature	Angle insensitive	Multi-physical quantity	Janus	Sensing performance		
				S THz per RIU	Q	FOM RIU^{-1}
This work	Forward 0–60°	Thickness	✓	27.07	38	140.3
	Backward 0–72.5°	Temperature		5.52	8.3	6.2
		Voltage		4.44	37.2	20.2
		Glucose		0.007	36.8	0.04
		Alcohol		940.34	37	4700
Ref. 46	✘	Thickness	✘	10	None	None
Ref. 47	✘	Glucose	✘	22	0.865	0.3865
Ref. 48	✘	Alcohol	✘	0.6677	None	None
Ref. 49	✘	Temperature	✘	0.01069	None	0.0218
Ref. 50	✘	Voltage	✘	7.35	None	None
Ref. 51	0–40°	Mechanochromic	✘	None	None	None
Ref. 52	0–60°	RI	✘	0.78	16	None
Ref. 53	✘	Plasmonic	✘	0.95	26.48	68
Ref. 54	✘	Permittivity	✘	0.48	16.24	None

LPS detects the five substances separately within the frequency range of 6–10 THz, as illustrated in Fig. 13(a), the absorption peaks were all greater than 0.9. The smoothness of the absorption curve attests to the superiority of the design, with peak values occurring in the 7–9 THz range. The equivalent RI of the five AL-based groups is provided in Table 2. As shown in Fig. 13(b), the RI of various substances is centered around 8.5 THz, with maximum transmissibility obtained at this frequency. In most regions, the frequency ranges of 6–7.5 THz and 9–10 THz are non-absorbable substances. Despite the uneven spacing of the RI of the selected substance, $f = -4.44n + 14.404$ in Fig. 13(c) demonstrates that a correlation coefficient of 0.999 can still be achieved by exploring the relationship between the RI and frequency, with an S value of 4.44 THz per RIU maintained. The specific fitting function is given by a mathematical expression. The high S and strong linear fitting degree can preliminarily indicate the rationality of the design structure used for alcohol differentiation. After S is defined, it can be used for further representation of sensor performance in combination with eqn (16)–(18). Moreover, Fig. 13(d) reveals that the performance of the sensor is adequate, with only slight fluctuations in the values of Q and FOM at the RI of 1.36, and an overall downward trend in the values of Q. When the FOM drops to the RI of 1.4, the average values of Q and FOM can reach 37.2 and 20.2 RIU^{-1}, with their data having standard deviations of 1.31 and 0.17.

Fig. 14(a) shows the simulated and calculated effect of $T_{External}$ on the absorption peak curve within the 6.5–8 THz range. Measurements are taken every 10 K between 259 K and 299 K. The results indicate a nearly constant shift of the curve with each $T_{External}$ change, $f = -0.007T + 5.38$ as illustrated in Fig. 14(c), suggesting a high S of the sensor to $T_{External}$ with a value of S = 0.007 THz K^{-1}. Additionally, Fig. 14(b) shows a distinct high absorption value within the working frequency range, with a linear reduction on both sides of the peak until it reaches 0 transmittance. These results provide a theoretical foundation for the development of the sensor. Fig. 14(d) presents the specific sensing performance, with a mean value of Q reaching 36.8 and the mean value of FOM sustained at 0.04 RIU^{-1}. Table 3 is used for comparison to showcase the design features of this paper. The sensor exhibits superior S, Q, and FOM compared to other sensors of the same type, while also allowing for the simultaneous measurement of three different physical quantities.

3. Conclusions

Generally speaking, this study proposed an angle-insensitive Janus graphene-based sensor capable of detecting multiple physical quantities, including thickness, graphene-applied voltage, $T_{External}$, G, and AL. The proposed LPS conducts a comprehensive performance analysis using the APSO-driven TMM, which enabled us to count the performance parameters of various sensors in both the front and rear directions. Our sensor demonstrated excellent performance in thickness detection, with values of S = 27.07 THz μm^{-1}, Q = 38, and FOM = 140.3 RIU^{-1}. Additionally, the voltage measurement performance is outstanding, with S, Q, and FOM values of 940.34 THz per RIU, 37, and 4700 RIU^{-1}. Notably, the sensor's absorption rate is higher than 0.9 in a wide range of angles due to the principle of phase matching, which is a splendid feature of this study. This paper attributes our success to the powerful multi-objective optimization function of the APSO algorithm, which helps us find optimal performance solutions in multiple iterations. The simplicity of the sensor's physical structure suggests that it has a wide range of practical applications, and we expect the APSO algorithm and HM-containing graphene layer to make further contributions to various scientific fields.

Conflicts of interest

There are no conflicts to declare.

Notes and references

1 S. Zaman, M. M. Hassan, M. Hasanuzzaman and M. Z. Baten, *Opt. Express*, 2020, **28**, 25007–25021.
2 S. G. Johnson and J. D. Joannopoulos, *Appl. Phys. Lett.*, 2000, **77**, 3490–3492.
3 N. Kumari, A. D. Varshney, S. K. Awasthi, L. Shiveshwari and A. H. Aly, *Phys. Plasmas*, 2022, **29**, 042110.

4 V. S. Chaudhary, D. Kumar and S. Kumar, *IEEE Trans. Plasma Sci.*, 2021, **49**, 3803–3810.
5 M. De, T. K. Gangopadhyay and V. K. Singh, *Sensors*, 2019, **19**, 464.
6 Z. A. Zaky, A. M. Ahmed, A. S. Shalaby and A. H. Aly, *Sci. Rep.*, 2020, **10**, 9736.
7 H. K. Baghbadorani and J. Barvestani, *Appl. Surf. Sci.*, 2021, **537**, 147730.
8 O. Temkin, *Chemical Reaction Networks: A Graph-Theoretical Approach*, JHU Press, 2006.
9 M. Sun and U. Schwingenschlogl, *Chem. Mater.*, 2020, **32**, 4795–4800.
10 H. Wang, S. Yang, S. N. Yin, L. Chen and S. Chen, *ACS Appl. Mater. Interfaces*, 2015, **7**, 8827–8833.
11 S. Wang, F. R. Pratama and M. S. Ukhtary, *Phys. Rev. B: Condens. Matter Mater. Phys.*, 2020, **101**, 081414.
12 S. Wang, C. Ren and H. Tian, *Phys. Chem. Chem. Phys.*, 2018, **20**, 13394–13399.
13 M. Sun, M. Re Fiorentin and U. Schwingenschlögl, *npj 2D Mater. Appl.*, 2022, **6**, 81.
14 S. Wang, M. S. Ukhtary and R. Saito, *Phys. Rev. Res.*, 2020, **2**, 033340.
15 X. L. Liu, R. Z. Zhang and Z. M. Zhang, *Appl. Phys. Lett.*, 2013, **103**, 213102.
16 I. V. Iorsh, I. S. Mukhin, I. V. Shadrivov, P. A. Belov and Y. S. Kivshar, *Phys. Rev. B: Condens. Matter Mater. Phys.*, 2013, **87**, 075416.
17 L. Ferrari, C. Wu, D. Lepage, X. Zhang and Z. Liu, *Prog. Quantum Electron.*, 2015, **40**, 1–40.
18 K. S. Novoselov, A. K. Geim, S. V. Morozov, D. E. Jiang, Y. Zhang and S. V. Dubonos, *Science*, 2004, **306**, 666–669.
19 A. K. Geim, *Science*, 2009, **324**, 1530–1534.
20 A. Ahmadivand, B. Gerislioglu and G. T. Noe, *ACS Appl. Electron. Mater.*, 2019, **1**, 637–641.
21 S. Yan, J. Adcock and Y. Ding, *Appl. Sci.*, 2021, **12**, 313.
22 W. Miao, L. Wang, X. Mu and J. Wang, *J. Mater. Chem. C*, 2021, **9**, 13600–13616.
23 Y. Liu, C. Ouyang, P. Zheng, J. Ma, Q. Xu, X. Su, Y. Li, Z. Tian, J. Gu, L. Liu and J. Han, *ACS Appl. Electron. Mater.*, 2021, **3**, 4203–4209.
24 S. Wicharn, S. Plaipichit, T. Seesan and P. Buranasiri, *SPIE*, 2018, **10516**, 233–243.
25 J. Sui, S. Liao, R. Dong and H. F. Zhang, *Ann. Phys.*, 2023, 2200661.
26 C. Li, M. Zhao, X. Zhou, H. Li, Y. Wang, X. Hu, M. Li, L. Shi and Y. Song, *Adv. Opt. Mater.*, 2018, **6**, 1800651.
27 L. L. Missoni, G. P. Ortiz, M. L. M. Ricci, V. J. Toranzos and W. L. Mochán, *Opt. Mater. Express*, 2020, **109**, 110012.
28 J. Kennedy and R. Eberhart, *IEEE*, 1995, **4**, 1942–1948.
29 B. S. Darki and N. Granpayeh, *Opt. Commun.*, 2010, **283**, 4099–4103.
30 M. Soruri, J. Sadri and S. Zahiri, *Anal. Appl.*, 2018, **21**, 1121–1126.
31 Y. Xu, Y. P. Tsai, K. N. Tu, B. Zhao, Q. Z. Liu and M. Brongo, *Appl. Phys. Lett.*, 1999, **75**, 853–855.
32 A. Pianelli, R. Kowerdziej, M. Dudek, K. Sielezin, M. Olifierczuk and J. Parka, *Opt. Express*, 2020, **28**, 6708–6718.
33 Y. Ma, T. Zhang, M. Mao, D. Zhang and H. Zhang, *Opt. Express*, 2020, **28**, 39890–39903.
34 S. Wang, N. T. Hung and H. Tian, *Phys. Rev. Appl.*, 2021, **16**, 024030.
35 H. Tian, C. Ren and S. Wang, *Nanotechnology*, 2022, **33**, 212001.
36 D. R. Smith, J. B. Pendry and M. C. Wiltshire, *Science*, 2004, **305**, 788–792.
37 B. F. Wan, Z. W. Zhou, Y. Xu and H. F. Zhang, *IEEE Sens. J.*, 2020, **21**, 331–338.
38 M. Clerc, *Randomness in Optimization*, John Wiley & Sons, 2010, p. 93.
39 H. Cao, H. Zhang, Z. Liu, Y. Zhou and Y. Wang, *IEEE*, 2021, 284–287.
40 B. F. Wan, Q. Y. Wang, H. M. Peng, H. N. Ye and H. F. Zhang, *IEEE Sens. J.*, 2021, **21**, 21465–21472.
41 P. Saeedi, I. Petersohn, P. Salpea, B. Malanda, S. Karuranga, N. Unwin, S. Colagiuri, L. Guariguata, A. A. Motala, K. Ogurtsova and J. E. Shaw, *Diabetes Res. Clin. Pract.*, 2019, **157**, 107843.
42 H. Liu, C. Chen, Y. Zhang, B. Bai and S. Tang, *Sensors*, 2019, **19**, 4803.
43 H. D. Holder, R. F. Saltz, J. W. Grube, R. B. Voas, P. J. Gruenewald and A. J. Treno, *Addiction*, 1997, **92**, S155–S171.
44 A. Panda and P. D. Pukhrambam, *Braz. J. Phys.*, 2021, **51**, 481–492.
45 K. Ahmed, M. J. Haque, M. A. Jabin, B. K. Paul, I. S. Amiri and P. Yupapin, *Phys. B*, 2019, **570**, 48–52.
46 A. Hassani and M. Skorobogatiy, *J. Opt. Soc. Am. B*, 2009, **26**, 1550–1557.
47 S. K. Chamoli, S. C. Singh and C. Guo, *IEEE Sens. J.*, 2020, **20**, 4628–4634.
48 B. K. Paul, M. S. Islam, K. Ahmed and S. Asaduzzaman, *Photonic Sens.*, 2017, **7**, 123–130.
49 M. M. Abadla, H. A. Elsayed and A. Mehaney, *Silicon*, 2021, **13**, 4737–4745.
50 Q. Liu, P. Xue and Z. Liu, *Appl. Phys. Express*, 2020, **13**, 032005.
51 G. Bae, M. Seo, S. Lee, D. Bae and M. Lee, *Adv. Mater. Technol.*, 2021, **6**, 2100118.
52 P. Qin, E. Li, T. Li, H. Ma, Y. Yang, L. K. Ang and H. Chen, *IEEE Trans. Microwave Theory Tech.*, 2020, **69**, 1511–1517.
53 B. Sun, Y. Yu and W. Yang, *Opt. Express*, 2020, **28**, 16605–16615.
54 Q. W. Ye, L. Y. Guo, M. H. Li, Y. Liu, B. X. Xiao and H. L. Yang, *Phys. Scr.*, 2013, **88**, 055002.

